Moho depth determination from waveforms of microearthquakes in the West Bohemia/Vogtland swarm area

Pavla Hrubcová,[1] Václav Vavryčuk,[1] Alena Boušková,[1] and Josef Horálek[1]

Received 3 April 2012; revised 6 November 2012; accepted 8 November 2012; published 17 January 2013.

[1] The West Bohemia/Vogtland area is known for its increased geodynamic activity with reoccurrence of intraplate earthquake swarms. Previous geophysical studies, namely active and passive seismic investigations, revealed a high velocity lower crust in this area with increased reflectivity. To refine this result and retrieve a more detailed structure of the deep crust and the Moho discontinuity, we analyzed waveforms of local microearthquakes that occurred in this area during the 2008 swarm. The waveforms of earthquakes were grouped into clusters with similar focal mechanisms, and the clusters were processed separately. We developed a new multiazimuthal approach in data processing to increase resolution of Moho phases in the waveforms. We applied the waveform cross-correlation of the *P* and *S* waves, and rotated, aligned, and stacked the seismograms to extract the Moho *SmS*, *PmP*, and *PmS* reflected/converted phases. These phases were inverted for laterally varying Moho depth by ray tracing and a grid search inversion algorithm. The model retrieved was verified using modeling of full waveforms computed by the discrete wave number method. The multiazimuthal approach reveals details in the velocity structure of the crust/mantle transition at each station. Instead of a single interface with a sharp velocity contrast, the inversion indicates a reflective zone at Moho depths with one or two strongly reflective interfaces, which is in agreement with the zone interpreted by previous investigations. The thickness of the zone varies from 2 to 4 km within the depth range of 27–31.5 km and is delimited by reflections from its top and bottom boundaries, sometimes with strong reflectors within the zone. The average V_p/V_s ratio determined from the Moho reflections and conversions is 1.73.

Citation: Hrubcová, P., V. Vavryčuk, A. Boušková, and J. Horálek (2013), Moho depth determination from waveforms of microearthquakes in the West Bohemia/Vogtland swarm area, *J. Geophys. Res. Solid Earth*, *118*, 120–137, doi:10.1029/2012JB009360.

1. Introduction

[2] The seismic velocity model within the Earth's crust is usually inferred from active seismic experiments, i.e., reflection and refraction seismic profiling, or from passive seismic experiments that are broadly focused on receiver function interpretations. However, though both investigations sample the same structure, the resultant velocity models often differ. The differences originate from different resolutions of the applied seismic methods, different frequency bands, spatial resolutions, or uncertainties in the V_p/V_s ratio. To improve the model and remove these inconsistencies, data from local microseismicity can be used as another source of information. The microseismic data are suitable namely for the following reasons: (1) high-frequency seismic waves generated by local sources are quite sensitive to inhomogeneities in the crust, and (2) microseismic observations often represent extensive datasets ideal for stacking. Thus, the structure can be investigated from reflected and/or converted phases secondarily generated at deep and shallow layers. With a good azimuthal distribution of local seismic stations densely covering the area it is even possible to detect lateral variations and topography of these layers.

[3] In this paper, we develop a new multiazimuthal approach to extract information on crustal structure from waveforms of local microearthquakes and test this approach on determining depth and lateral variations of the Moho discontinuity. Since focal mechanisms control the wave polarization and the shape of waveforms of local microearthquakes, a good azimuthal coverage of stations is required and proper attention must be paid to polarizations and radiation patterns of the studied waves. For this reason, we work in the so-called multiazimuthal regime. We analyze data in many differently oriented coordinate systems in order to find an optimal system, in which the studied reflected/converted waves displayed the best resolution. We show that the data rotation into the multiazimuthal sections is

[1]Institute of Geophysics, Academy of Sciences, Boční II/1401, 141 31 Prague 4, Czech Republic.

Corresponding author: P. Hrubcová, Institute of Geophysics, Academy of Sciences, Boční II/1401, 141 31 Prague 4, Czech Republic. (pavla@ig.cas.cz)

2169-9313/13/2012JB009360

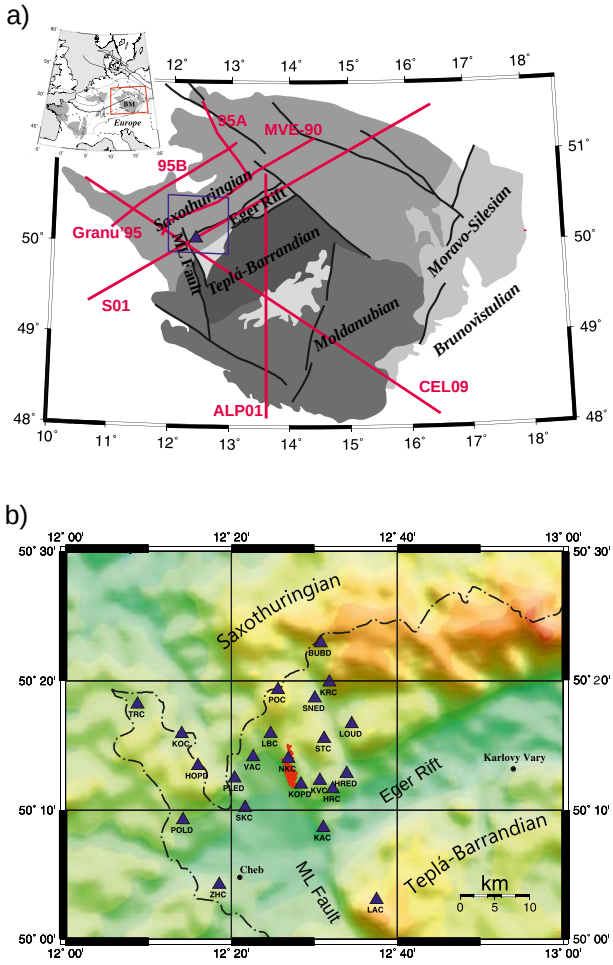

Figure 1. (a) Simplified tectonic units of the Bohemian Massif (BM) with major seismic profiles (red lines). (b) Topographic map of the West Bohemia/Vogtland region. Seismic stations of the WEBNET network are marked by blue triangles; hypocenters of local microearthquakes of 2008 swarm are marked by red dots. ML Fault, Mariánské Lázně Fault.

necessary to enhance details of the crustal structure. In addition, we apply a combination of several other tools in the data processing: data alignment and stacking, ray tracing for calculation of the synthetic arrival times of the reflected/converted phases, analysis of the reflection/transmission coefficients in order to assess the amplitudes of the reflected/converted phases and their resolution in real waveforms, synthetic modeling of full waveforms with the discrete wave number method to compare synthetic wavefields with recorded data, and the grid search algorithm as a robust inversion method for depth determination of crustal discontinuities.

[4] The tools developed for passive microseismic investigation of the crustal structure are applied to the West Bohemia/Vogtland region, the western part of the Bohemian Massif (Figure 1). This area is known for intense seismicity characterized by reoccurrence of intraplate earthquake swarms. The seismicity is located in the upper and middle crust down to about 20 km depth [*Fischer and Horálek*, 2003]. The seismic activity is monitored by the West Bohemia Network (WEBNET) of local seismic stations, densely covering the whole area (Figure 1) and providing high-quality observations, which perfectly suit the above mentioned needs of our study. We apply the multiazimuthal approach in order to disclose details in the Moho discontinuity in this area, the structure of which is particularly important from a tectonic point of view. Since intraplate earthquake swarms without active volcanism are unusual and occur mainly in areas of enhanced crustal fluid activity [*Horálek et al.*, 2000], detailed knowledge of crustal structure is essential for understanding this specific geodynamically active region.

2. Geological and Geophysical Setting

2.1. Geology and Tectonic Evolution of the Region

[5] The Bohemian Massif is one of the largest stable outcrops of pre-Permian rocks in Central and Western Europe. It forms the easternmost part of the Variscan orogenic belt, which developed approximately between 500 and 250 Ma during a period of large-scale crustal convergence, collision of continental plates and microplates, and subduction [*Matte et al.*, 1990]. The West Bohemia/Vogtland region (Figure 1) forms the western part of the Bohemian Massif and it is situated in the transition zone among three different Variscan structural units: the Saxothuringian in the northwest, the Teplá-Barrandian in the central region, and the Moldanubian in the southeast [*Babuška et al.*, 2007]. The Paleozoic suture between the Saxothuringian and Teplá-Barrandian/Moldanubian units has been reactivated since the Upper Cretaceous/Tertiary, which led to the evolution of the 300 km long and 50 km wide NE-SW trending Eger Rift, which is an active element of the European Cenozoic Rift System [*Prodehl et al.*, 1995]. The area is also intersected by the NNW-SSE striking Mariánské Lázně fault and an active fault system trending N-S [*Bankwitz et al.*, 1997].

[6] The West Bohemia/Vogtland area as the western part of the Eger Rift (Figure 1) is known for its increased geodynamic activity represented by seismicity, numerous mineral springs, CO_2 emissions, Tertiary/Quaternary volcanism, and neotectonic crustal movements located at the intersections of fault zones [*Weinlich et al.*, 1999]. The seismicity is manifested by a reoccurrence of intraplate earthquake swarms with local magnitude of mostly less than 4 [e.g., *Fischer and Horálek*, 2003; *Horálek et al.*, 2009], though the strongest documented earthquakes occurred during the swarms of 1872 and 1908 and reached the magnitude of about 5.0. So far, the largest instrumentally recorded swarm was in 1985/86 and the strongest event reached a magnitude of 4.6 [*Vavryčuk*, 1993]. The seismicity is relatively shallow with the hypocenters of the events located in the upper and middle crust down to about 20 km depth with the majority between 5 and 15 km [*Fischer and Horálek*, 2003].

2.2. Previous Geophysical Investigations in the West Bohemia/Vogtland Area

[7] The structure of the crust and the crust-mantle boundary in the West Bohemia region has been a target of several seismic experiments over the last 25 years. Active seismic studies

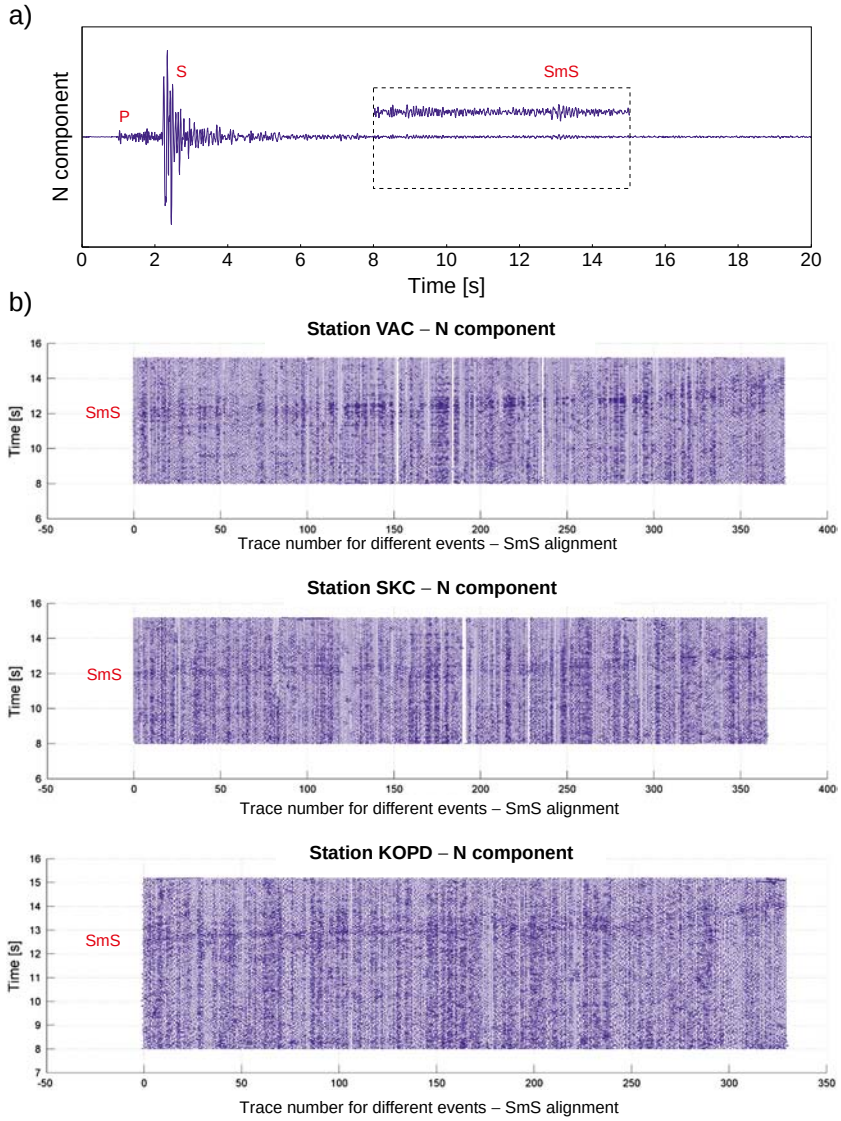

Figure 2. Data. (a) The *N* component of the velocity record of the event 6774A, from 21 October, 2008, M_L of 1.1, at station KOPD. Dashed rectangle shows the time window for zooming of *SmS* phases. (b) Velocity records showing the aligned Moho reflected *SmS* phase for the whole data set of earthquakes with a similar mechanism.

comprised of reflection experiments such as DEKORP-4/KTB, MVE-90, 9HR [*DEKORP Research Group*, 1988; *Behr et al*., 1994; *Tomek et al*., 1997] as well as refraction and wide-angle reflection experiments as GRANU'95 [*Enderle et al*., 1998], CELEBRATION 2000 with CEL09 profile [*Hrubcová et al*., 2005], ALP 2002 with ALP01 profile [*Brückl et al*., 2007], and SUDETES 2003 with S01 profile [*Grad et al*., 2008]. Passive seismic experiments with permanent and temporary seismic stations were performed to study major lithospheric discontinuities with the application of the receiver functions [*Geissler et al*., 2005; *Wilde-Piórko et al*., 2005; *Heuer et al*., 2006].

[8] Modeling of refraction and wide-angle reflection profile CEL09 of the CELEBRATION 2000 experiment revealed a highly reflective top of the lower crust at a depth of 27–28 km [*Hrubcová et al*., 2005]. These results

Table 1. 1-D Velocity Profile Used for Calculation of Ray-Tracing, Synthetic Full Wave Fields, and for the Moho Depth Determination

Depth of Layer [km]	Vp [km s^{-1}]
0.0	4.30
0.2	5.06
0.5	5.33
1.0	5.53
1.5	5.66
2.0	5.87
4.0	6.09
6.0	6.27
7.0	6.43
15.0	6.85
30.0	8.10

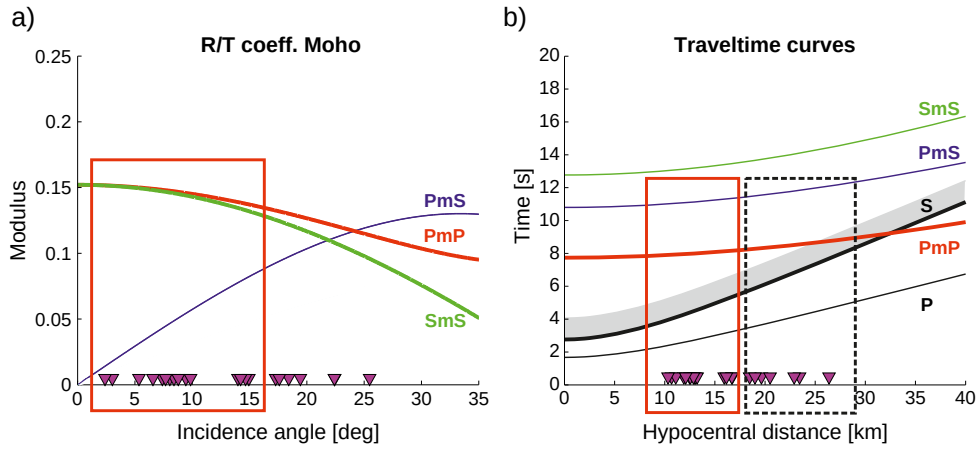

Figure 3. Analysis of detectability of the *PmP* phases. (a) *R*/*T* coefficients. Stations are plotted according to their *PmP* or *SmS* incidence angles, which is proportional to the epicentral distance. (b) Traveltime curves for *P*, *S*, *PmP*, *PmS*, and *SmS* phases calculated for a 1-D velocity model with a source at zero epicentral distance and at a depth of 10 km. Moho is at a depth of 30 km. Note overlapping of the *PmP* traveltime curve with the *S* wave coda (grey rectangle) for more distant stations (highlighted by dotted black rectangle). Red rectangles show WEBNET stations suitable for the interpretation of *PmP* phases. Station positions are marked by magenta triangles.

corresponded to the reflection profile MVE-90, where the Moho was interpreted at 10 s two-way-time at the bottom of 5–6 km thick reflective lower crust [*DEKORP Research Group*, 1994]. The GRANU'95 results indicated the existence of a high-velocity layer at the base of the crust in the Saxothuringian zone in SE Germany with a velocity increase from 6.5 km s^{-1} in the middle crust to an average value of 7.0 km s^{-1} at a depth of 24 km, which was interpreted as the top of the lower crust [*Enderle et al.*, 1998].

[9] The receiver function teleseismic studies observed converted waves from the base of the crust at about 3.7 s. Assuming constant average crustal velocity V_p of 6.3 km s^{-1} and V_p/V_s ratio of 1.73, *Geissler et al.* [2005] interpreted the depth of the Moho discontinuity to be at about 31 km. Underneath the western part of the Eger Rift, a delay time of only 3.0–3.3 s was interpreted as a thinning of the crust to about 27 km. Similar results were achieved by *Heuer et al.* [2006] who used receiver functions with a dense seismic network and restricted the Moho upwelling to the SW termination of the Eger Rift.

[10] The differences in the Moho depth estimated by active and passive seismic investigations could be explained, to some extent, by the different resolutions of these methods, by different frequency bands and spatial resolutions and/or the uncertainty in the V_p/V_s ratio. *Hrubcová and Geissler* [2009] discussed these inconsistencies and showed that the

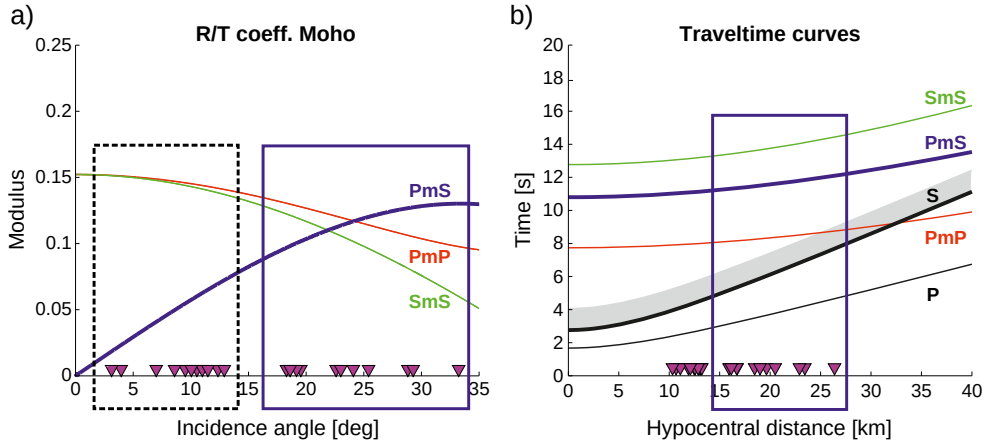

Figure 4. Analysis of detectability of the *PmS* phases. (a) *R*/*T* coefficients. Stations are plotted according to the *PmS* incidence angle, which is proportional to the epicentral distance. (b) Traveltime curves for *P*, *S*, *PmP*, *PmS*, and *SmS* phases calculated for a 1-D velocity model with the source at zero epicentral distance and at a depth of 10 km. Moho is at a depth of 30 km. Note very low *R*/*T* coefficients for near vertical stations (highlighted by dotted black rectangle). Blue rectangles show WEBNET stations suitable for interpretation of *PmS* phases. Station positions are marked by magenta triangles.

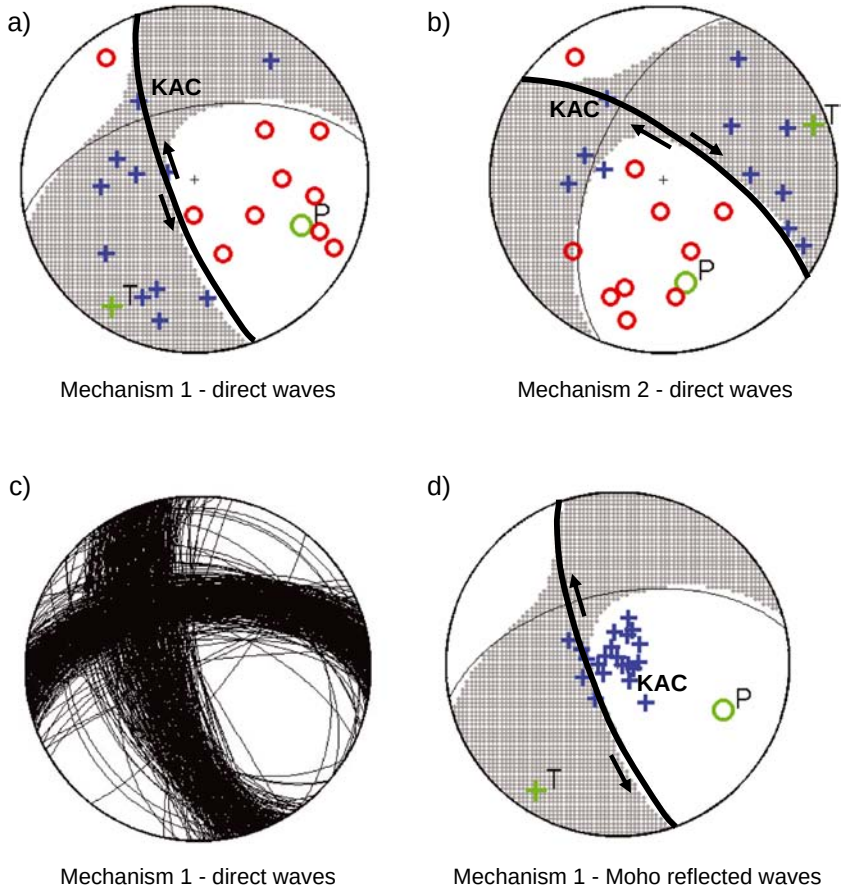

Figure 5. Two focal mechanisms characteristic for the swarm 2008 with projection of the WEBNET seismic stations (marked by red circles and blue crosses). (a) Focal mechanism of the first type (observed for 90% of all events). Positions of stations correspond to take-off angles of the direct waves. (b) Focal mechanism of the second type. Positions of stations correspond to take-off angles of the direct waves. Note that station KAC is located at the crossing of the nodal planes for both mechanisms and thus has the least favorable position from all WEBNET stations. (c) Focal mechanisms of all analyzed events of the 2008 swarm. Apparent misfit of the nodal planes is a result of focal mechanism interpretation. (d) Focal mechanism of the first type. Positions of stations correspond to take-off angles of the Moho reflected waves.

synthetic modeling of receiver functions allows for a lower crustal layer (or gradient zone) of about 5 km thickness instead of a single first-order discontinuity. Joint modeling of the seismic refraction data and receiver functions in the West Bohemia/Vogtland region resulted in a model with the top of the lower crust at a depth of 28 km, where the high reflectivity obscured weaker Moho reflections at a depth of ~32–33 km.

3. Data

3.1. The 2008 West Bohemia Earthquake Swarm

[11] To detect seismic velocities and the Moho depth in the West Bohemia/Vogtland region, we used waveforms of local microearthquakes that occurred during the 2008 swarm. This swarm lasted for 4 weeks and involved about 25,000 microearthquakes with magnitudes higher than –0.5. The largest earthquake reached a magnitude of 3.7 [*Horálek et al*., 2009; *Fischer et al*., 2010]. The microearthquakes were recorded at 22 seismic stations of the local seismic network WEBNET densely covering the area with epicentral distances up to 25 km (Figure 1). The sampling rate was 250 Hz. Focal depths of the events were among 7.6 km and 11.7 km determined with relative accuracy on the order of 100 m from the relative double-difference location method.

[12] The focal mechanisms of the events were of two types and pointed to activation of two different fault systems. The majority of the events occurred along the fault oriented nearly in the N-S direction with the strike of 169° [*Vavryčuk*, 2011a, 2011b, 2011c]. This fault was characterized by occurrence of oblique left-lateral strike slip with a weak normal component. The other fault was oriented in the WNW direction with the strike of 304° and displayed oblique right-lateral strike-slip mechanisms with a weak normal component. This fault was less active and only a small portion of events occurred along it. The maximum compressive stress in the region determined from the focal mechanisms was in a NW-SE direction with an azimuth of 146° [*Vavryčuk*, 2011a].

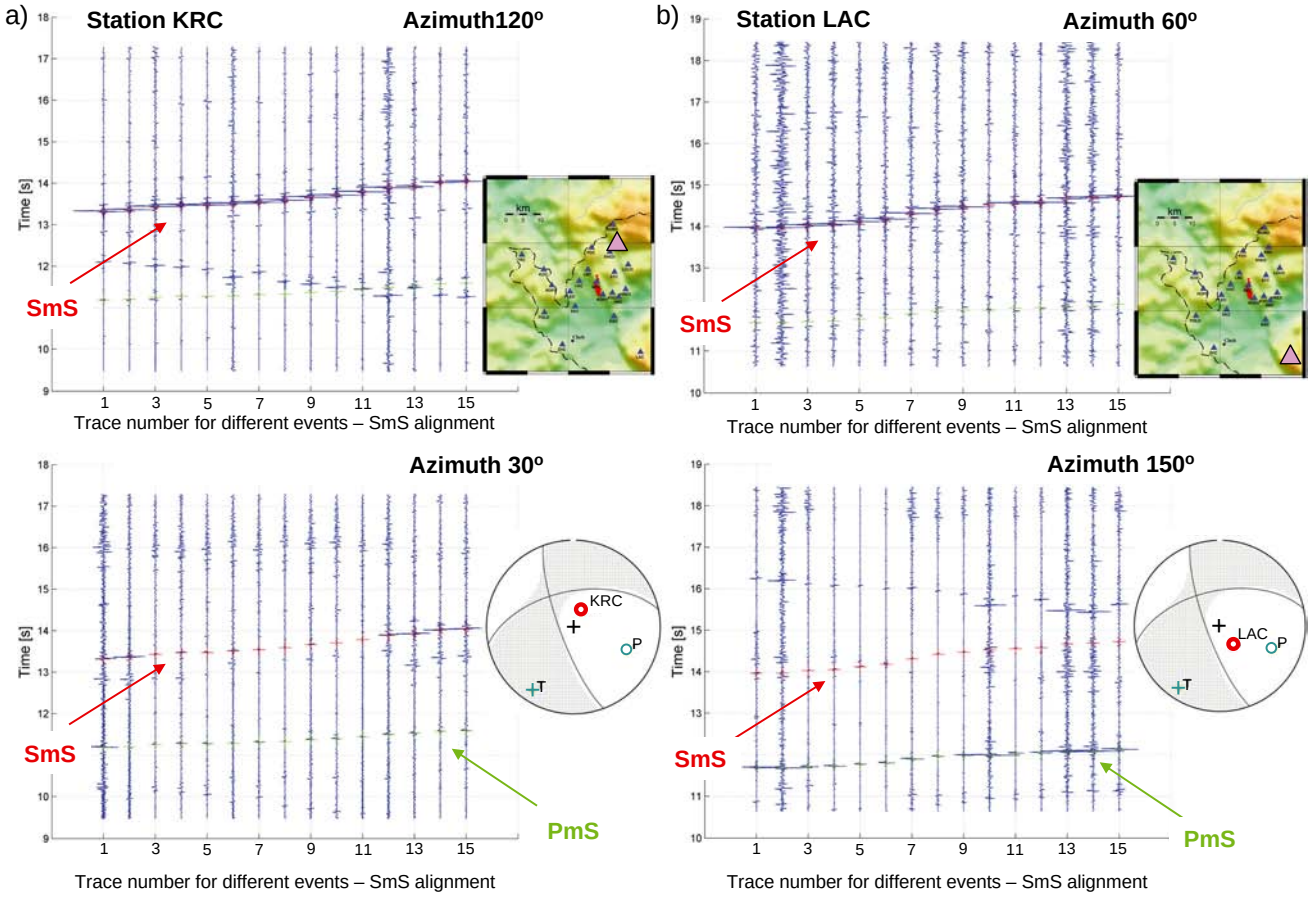

Figure 6. Synthetic seismograms for 15 events of the first type (strike of 169°, dip of 68°–80°, and rake of –44°) calculated with discrete wave number method and rotated into different azimuths. Hypocenters located at the depths among 7.6–10.7 km; seismograms aligned according to the time of the Moho reflected *SmS* phase for each event; no noise applied. (a) Station KRC located to the NNE from the epicentral area. Note strong *SmS* phase for the azimuth of 120° and less pronounced *SmS* phase for the azimuth of 30° (both marked by red arrows). (b) Station LAC located to the SE from the epicentral area. Note strong *SmS* phase for the azimuth of 60° and almost missing *SmS* phase for the azimuth of 150° (both marked by red arrows). Green arrows mark *PmS* phase, which is pronounced at station LAC, azimuth 150° (Figure 6b bottom) and less pronounced at station KRC, azimuth 30° (Figure 6a bottom). Position of stations in the geographical map is marked by a pink triangle. Focal sphere with projection of station for Moho reflected take-off phases and *P*, *T* axes indicated.

3.2. Data Processing

[13] We used 470 events recorded at the majority of the WEBNET seismic stations, which resulted in processing of more than 9000 waveforms and ensured sufficient azimuthal coverage. The waveforms were band-pass filtered (usually between 0.5–25 Hz), which eliminated low- and high-frequency noise. The waveforms typically displayed dominant direct *P* and *S* waves followed by converted and reflected waves secondarily generated at deep and shallow structures (Figure 2a).

[14] To extract various converted and reflected phases within the crust, namely those related to the Moho discontinuity, we applied the waveform cross-correlation of the direct *P* waves and this enabled to detect their precise onsets in the waveforms. These onsets were applied for the primary waveform alignment (Figure 2b) and then associated with the traveltimes calculated by ray tracing. In order to remove the effects of local structure beneath each station, the traveltimes of the Moho reflected/converted phases were calculated relative to the direct *P* waves. These traveltimes also served for the alignment of traces to enhance visibility of the Moho reflected/converted phases in seismograms.

[15] In the stacking procedure, when calculating the theoretical traveltimes of the Moho phases, we varied two parameters: the velocity in the focal zone and the Moho depth. The velocities and depths of the other layers in the velocity model (Table 1) were fixed. For each combination of these parameters, we aligned the waveforms according to the calculated arrival times of the *SmS*, *PmP*, or *PmS* phases, respectively, and stacked them in order to amplify the coherently arrived reflection/conversion Moho phases. The data were processed for each station separately to evaluate lateral variations in the depth of the crust-mantle boundary. The specific values used in the grid search inversion are described in the next sections.

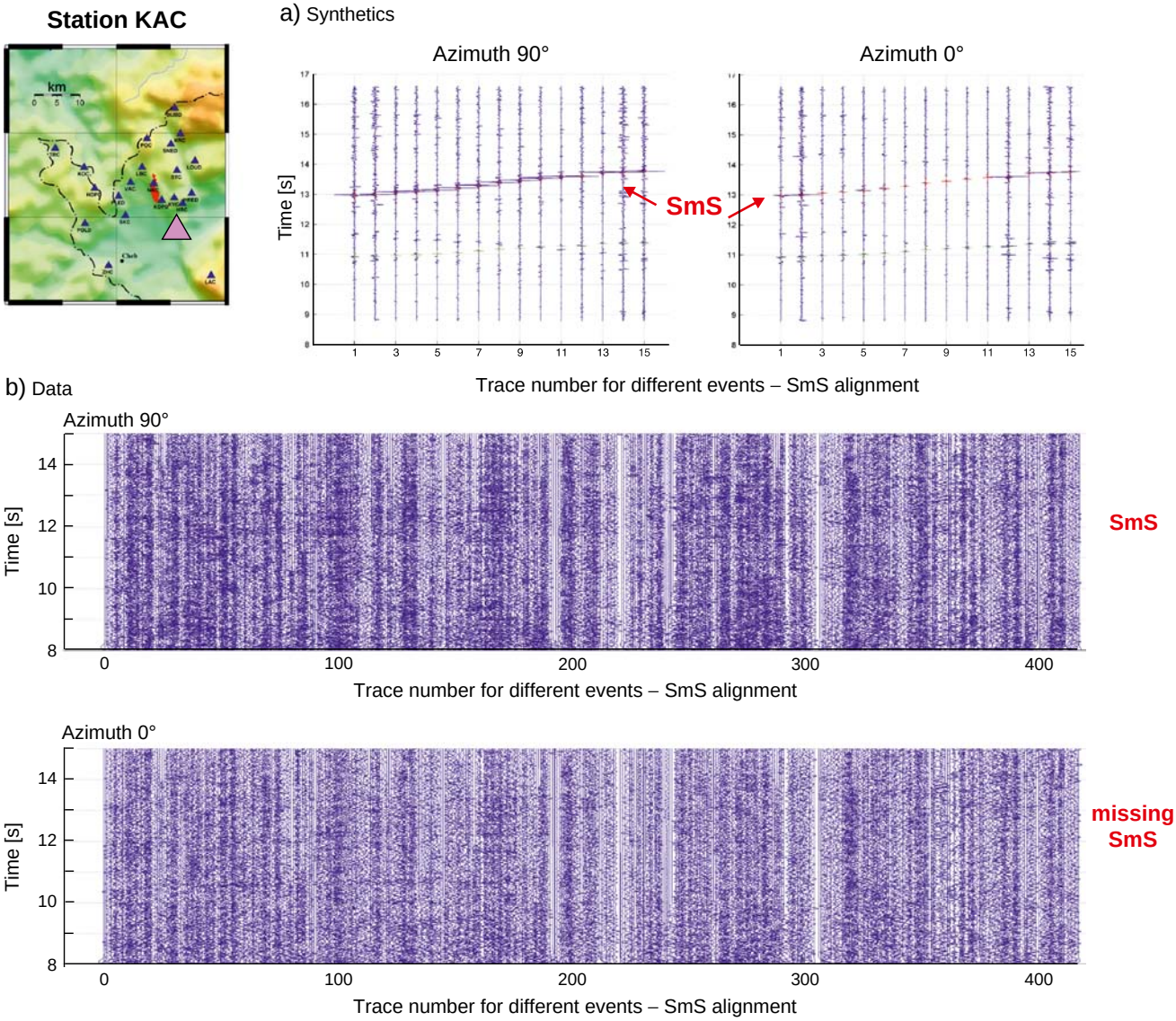

Figure 7. Synthetics and data at station KAC (epicentral distance ~10 km) rotated into azimuths of 0° and 90° to show differences in the *SmS* energy for the optimum and perpendicular azimuths. (a) Synthetic seismograms for 15 events of the first type calculated using discrete wave number method. (b) Sections of the horizontal velocity records of all analyzed events. Synthetic seismograms and velocity records are aligned according to the time of the Moho reflected *SmS* phase for each event (for earthquakes with similar focal mechanisms). Note pronounced Moho *SmS* reflections for azimuth 90° (optimum azimuth) but missing energy for the *SmS* reflections for azimuth 0° corresponding with the synthetics. Position of station KAC in the geographical map is marked by a pink triangle.

3.3. Selection of Suitable Stations

[16] The *SmS* phases were reasonably pronounced and well-separated from the *S*-wave coda at all WEBNET stations. The other Moho reflected and converted phases were weaker; hence a detailed analysis of theoretical traveltime curves and of the reflection/transmission (*R*/*T*) coefficients was necessary to identify them reliably. Figure 3 shows a selection of stations for the interpretation of the *PmP* phase. Synthetic traveltime curves of the *P*, *S*, *PmP*, *PmS*, and *SmS* phases were calculated for a one-dimensional (1-D) velocity model (Table 1) with the source at a depth of 10 km and the Moho at a depth of 30 km. The *R*/*T* coefficients for the *PmP* phase are sufficiently high within the whole range of epicentral distances (Figure 3a). However, the traveltime curves show overlapping of the *PmP* phase with the *S*-wave coda for more distant stations (Figure 3b). Therefore, such stations were excluded from the *PmP* interpretation. Similar analysis was done for the converted *PmS* phase (Figure 4). The traveltime curves do not show any overlapping of the *PmS* phase with other phases. However, near stations with almost vertical incidences were excluded from the *PmS* interpretation because of very small *R*/*T* coefficients. Thus, finally, distant stations (hypocentral distance among ~14–28 km) are mostly considered for the interpretation of the *PmS* phases and near stations (hypocentral distance

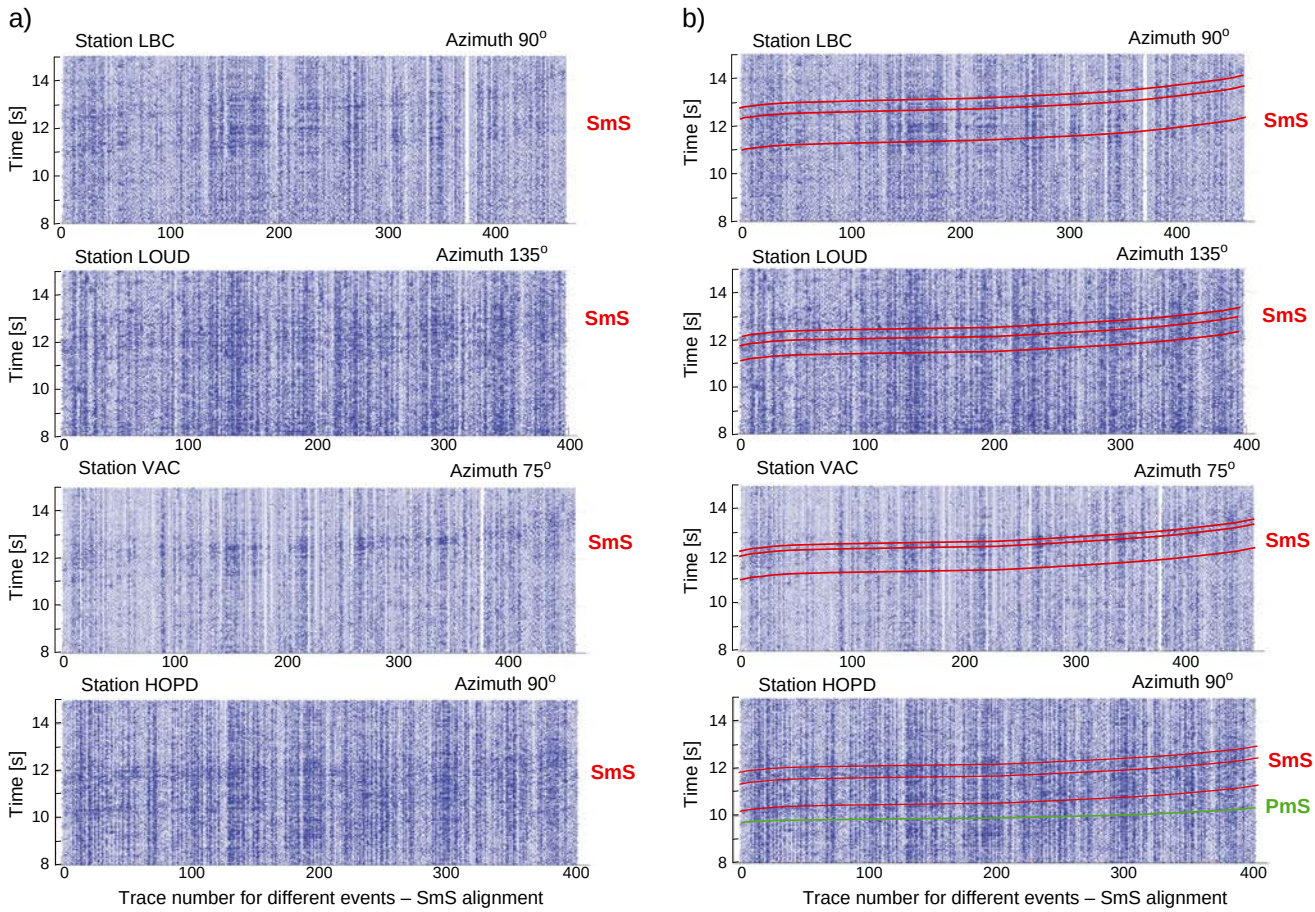

Figure 8. (a) Data sections rotated into optimum azimuths for the *SmS* phases. Sections of the horizontal velocity records of all analyzed events at stations LBC, LOUD, VAC, and HOPD. The records are aligned according to the time of the Moho reflected *SmS* phase for each event (for earthquakes with similar focal mechanisms) and rotated into optimum azimuths with maximum energy for the Moho *SmS* phase. Instead of sharp Moho reflections a reflective zone is visible in the data sometimes with more than one strongly reflective interface. (b) The same data sections for the Moho *SmS* phases as in Figure 8a with superimposed traveltimes calculated using ray tracing (red lines). Traveltime curves interpreted at 27.5 km, 30.5 km, and 31 km (station LBC); at 28 km, 29.5, and 30.5 km (station LOUD); at 27.5 km 29.75 km, and 30.25 km (station VAC); at 26.75 km, 29.25 km, and 30.5 km (station HOPD). Note *PmS* phase at station HOPD interpreted at 30.5 km (green line).

among ~10–17 km) are mostly considered for the interpretation of the *PmP* phases.

4. Synthetic Tests – Numerical Modeling for Radiation Pattern

[17] Amplitudes of converted and reflected waves in waveforms of local microearthquakes significantly depend on focal mechanisms and on the source-receiver geometry. This is specific for microseismic data; it complicates their analysis and it is usually absent in processing of other types of data. For example, in active experiments the sources have rather uniform radiation pattern, and in passive experiments the focal mechanisms of regional or teleseismic earthquakes affect the waveforms at stations in a very similar way. Therefore, when studying data from local seismicity, we have to pay more attention to analysis of focal mechanisms.

[18] Figures 5a and 5b show the positions of stations on the focal sphere together with two principal focal mechanisms characteristic for the analyzed seismicity [*Vavryčuk*, 2011c]. The figure shows that the stations have quite different positions with respect to the nodal lines and *P*/*T* axes for both mechanisms. Moreover, the station positions on the focal sphere differ for direct waves and for the Moho reflected waves (Figure 5d). This implies that reflected phases at some stations can be more visible in waveforms of events with the focal mechanism of the first type than with the focal mechanism of the second type. Therefore, we have to carefully check the data especially when there are some weak reflections and distinguish between two cases. First, a weak reflection can indicate an absence of a strong-contrast interface. However, it can also represent a result of an unfavorable radiation produced by the actual focal mechanism, the source-receiver geometry, and unfavorable incidence angles at an interface.

[19] The sensitivity of the waveforms and particularly of the amplitudes of the Moho reflected waves to the focal mechanisms was confirmed by synthetic tests with the discrete wave

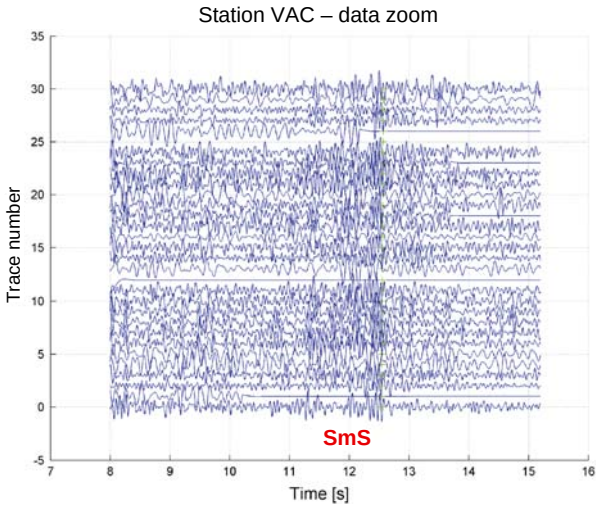

Figure 9. Detailed view of the horizontal velocity records at station VAC aligned and rotated into the optimum azimuth with maximum energy for the Moho reflected *SmS* phase. Note a reflective zone instead of sharp Moho reflections in time of 11.3–12.5 s.

number method [*Bouchon*, 1981]. In order to simulate real data as close as possible, we computed waveforms of 15 events located at depths ranging from 7.6 km to 10.7 km. The focal mechanisms were of the first type with strike, dip, and rake angles within the range of 169°, 68°–80°, –44°, respectively [*Vavryčuk*, 2011c]. We used the actual source-receiver geometry and the 1-D isotropic velocity structure with a sharp velocity contrast at the Moho discontinuity (Table 1). The full synthetic waveforms disclosed that the Moho *SmS* reflected phases were pronounced at horizontal components rotated into some specific azimuths. In other, unfavorable azimuths, the *SmS* reflected phases were less pronounced or even invisible. The azimuths showing the best resolution varied for each station and for each type of the focal mechanisms.

[20] Figure 6 documents the *SmS* alignment of synthetic waveforms at two stations rotated into two different azimuths. Station KRC located to the NNE of the foci featured a strong *SmS* phase for an azimuth of 120° and a less pronounced *SmS* phase for an azimuth of 30°. Station LAC located to the SE of the foci showed a strong *SmS* phase for an azimuth of 60° and a less pronounced *SmS* phase for an azimuth of 150°, for which the Moho converted *PmS* phase was quite pronounced. Hence, the modeling reveals that the synthetic waveforms are quite sensitive to a coordinate system into which the reflected/converted phases are rotated and in which they are studied. This specific phenomenon must be taken into account when processing real observations of local seismicity. Since this phenomenon relates to radiation pattern and source-receiver geometry, it is advantageous to process the waveforms separately for clusters of earthquakes with similar focal mechanisms.

5. Interpretation and Results

5.1. Multiazimuthal Analysis

[21] As illustrated above, the synthetic tests revealed a strong dependence of amplitudes of the Moho reflections/conversions on the focal mechanisms, radiation pattern, and the source-receiver geometry of local earthquakes. This is also confirmed in the analysis of real observations. As an

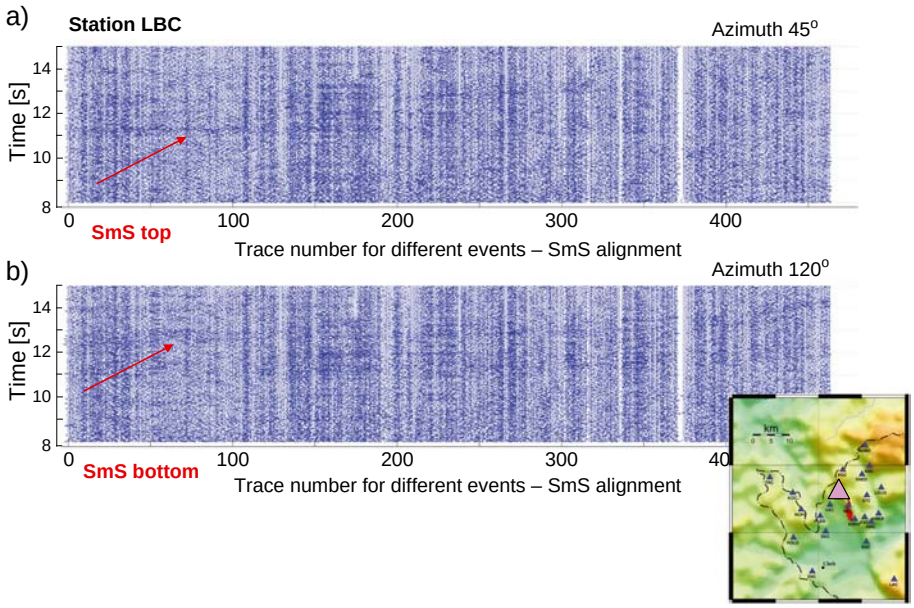

Figure 10. Sections with the *SmS* reflections pronounced at different depths in different azimuths. Sections of the horizontal velocity records of all analyzed events at station LBC; the records are aligned according to the time of the Moho reflected *SmS* phase for each event. (a) Pronounced Moho reflections from the top of the reflective zone in azimuth 45°. (b) Pronounced reflections from the bottom of the reflective zone in azimuth 120° (both marked by red arrows). Note that both azimuths are in directions of *R* and *T* components, which do not correspond to the optimum azimuths for this station (90° and 0°, respectively). Position of station LBC in the geographical map is marked by a pink triangle.

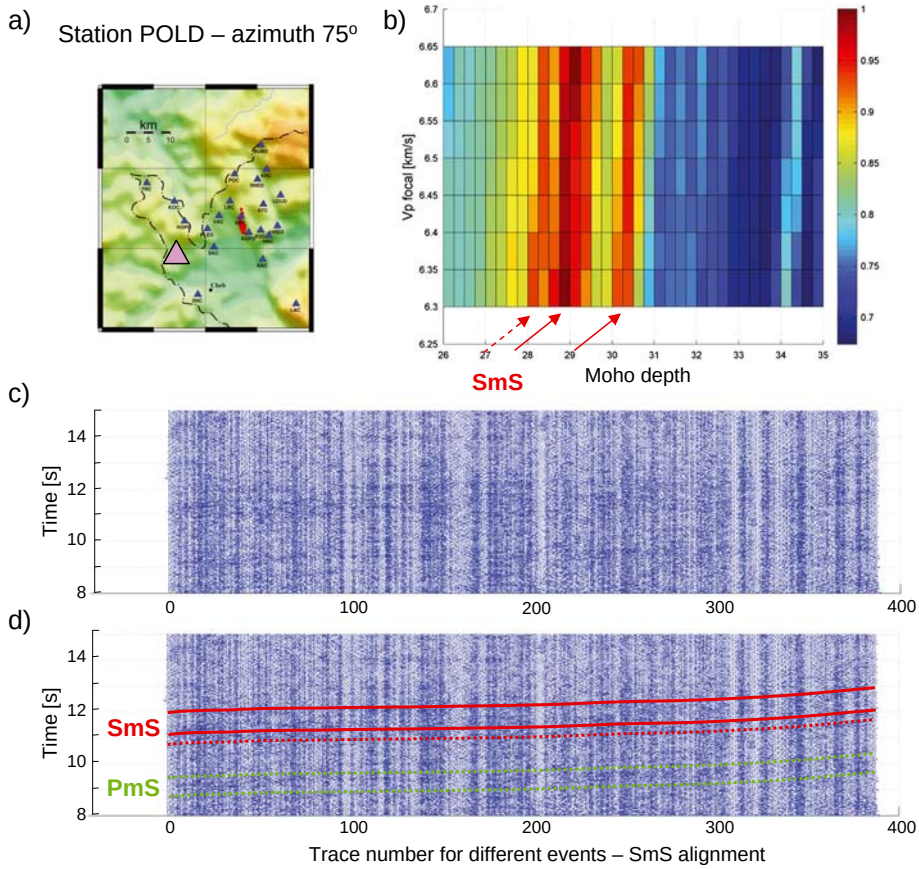

Figure 11. Inversion of the *SmS* reflections for the Moho depth at station POLD using horizontal velocity records rotated into the optimum azimuth of 75°. (a) Map of the area with station POLD marked by a pink triangle. (b) Stacked and inverted S*mS* phases with the grid search algorithm. The scale of the plot is normalized to the maximum amplitude of the stack; high values of the stack indicate strongly reflecting interface. The inversion reveals Moho reflections at the depths of ~28.0, 29.0, and 30.5 km, which correspond to the zone of an increased reflectivity in times between ~11–12 s. (c) Moho reflected *SmS* phases in the data with a wide reflective zone instead of a single sharp contrast at the Moho. (d) Moho reflected *SmS* phases in the data with traveltime curves calculated using ray tracing (red lines). Note Moho converted *PmS* phases indicated for the two most pronounced interfaces at the depths of 29.0 and 30.5 km (green lines).

example, Figure 7 shows two sections of the horizontal velocity records of all analyzed events at station KAC rotated into azimuths of 0° and 90°. Records for this station (epicentral distance ~10 km) show pronounced Moho *SmS* reflections for azimuth 90°, which is the optimum azimuth obtained from the synthetics, but missing energy for the *SmS* reflections for azimuth 0°.

[22] Therefore, a detailed analysis of real data and the Moho depth inversion were performed simultaneously in many coordinate systems rotated in the horizontal plane and defined by an azimuth varying from 0° to 180° with a step of 15°. The rotation was applied to all stations of the WEBNET network and enabled us to obtain preferential azimuths for the optimal resolution of the Moho phases at individual stations. Using the multiazimuthal approach we were able to reveal details in the velocity structure of the crust/mantle transition at each station unseen when we analyzed the data in the standard RTZ (radial, transversal, and vertical) coordinate system.

[23] The results of the multiazimuthal analysis obtained for four selected stations are shown in Figure 8. The figure indicates that instead of a sharp onset of one *SmS* phase, several onsets of the *SmS* phase are detected in the data (Figure 9). Moreover, the Moho *SmS* reflections at some stations are pronounced at different depths if analyzed in waveforms rotated into different azimuths (Figure 10). Such complex wavefields suggest the existence of a wide reflective zone with one or several strongly reflecting interfaces instead of a simple Moho with a sharp velocity contrast.

5.2. Moho Depth Inversion of the *SmS* Phase

[24] The inversion of the *SmS* phases for the Moho depth was performed in the following way. The horizontal components of the *SmS* phases were rotated into all multiazimuthal sections, and subsequently aligned and stacked. The arrival times of the stacks of the *SmS* phases at individual stations were inverted for laterally varying Moho depths using two-point ray tracing. The ray paths were calculated for the 1-D velocity model of *Málek et al*. [2005] simplified into a layered model with constant velocities (Table 1). The same 1-D velocity model was applied to locate hypocenters of the events. In the inversion, a robust grid search algorithm was

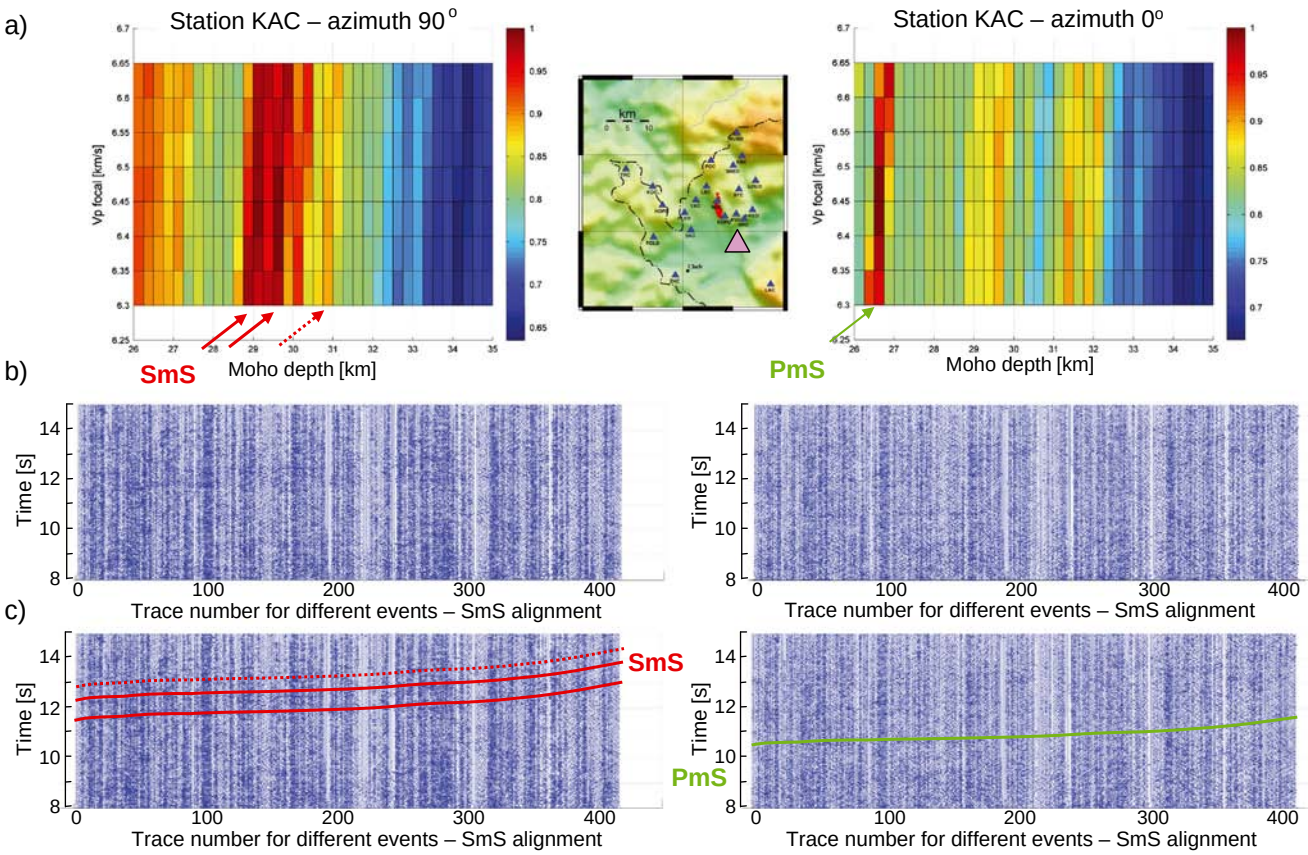

Figure 12. Inversion of the *SmS* reflections for the Moho depth at station KAC. The horizontal velocity records are rotated into azimuths 90° (left panels) and 0° (right panels). Note strong *SmS* reflections for azimuth 90° (left panels) and dying out of energy for azimuth 0° (right panels). (a) Stacked and inverted *SmS* phases with the grid search algorithm. The scale of the plot is normalized to the maximum amplitude of the stack. (b) The Moho-reflected *SmS* phases in the data. (c) Moho-reflected *SmS* phases in the data with traveltime curves calculated using ray tracing (29 and 30 km–solid red line, 31 km–dashed red line). Position of station KAC in the geographical map is marked by a pink triangle. Note maximum inversion for azimuth 0° at 26.5 km, which represents *PmS* phases instead of *SmS* phase from shallower Moho (green line).

used for finding two parameters: the Moho depth and the focal layer velocity. The grid step of the Moho depth was 0.250 km and the grid step of the focal layer velocity was 0.05 km s^{-1}. The inversion was performed for each station and for the whole set of azimuths. Then, the optimum azimuth was selected and the corresponding Moho depth was assigned to each station. Finally, lateral variations of the Moho depth in the region was obtained by interpolating depths of the Moho inverted for the individual WEBNET stations.

[25] The inversion of the *SmS* phases is illustrated for the station POLD (Figure 11); the scale of stacks in the inversion is normalized to the maximum amplitude. The results of the inversion are plotted together with the data to document how maxima of stacks correspond with the pronounced *SmS* energy in the data. The inversion reveals the Moho reflections at the depths of ~28.0, 29.0, and 30.5 km, which correspond to the zone of increased reflectivity in times between ~11–12 s. As mentioned above, such results disclose a wide reflectivity zone instead of a single sharp contrast at the Moho. Figure 11 also documents the Moho converted *PmS* phases in data for the two most pronounced interfaces at the depths of 29.0 and 30.5 km. This confirms the hypothesis of a zone with at least two pronounced interfaces.

[26] The advantage of the multiazimuthal analysis is illustrated in Figure 12, where sections of traces are rotated into different azimuths and presented together with the results of the inversion. Strong *SmS* reflections at station KAC for azimuth 90° and missing energy from Moho phases for perpendicular azimuth 0° are in agreement with the synthetics (Figure 7). Similarly, the multiazimuthal approach also performed well for other stations. In a few cases, the rotation of the data did not help in increasing the resolution of the Moho phases, and finding the optimal azimuth with the most pronounced energy was difficult. This happened mainly at the stations close to the epicenters and in directions close to the strike of the fault (e.g., stations VAC, LBC, or KOPD). The waveforms at these stations were quite sensitive even to small variations in focal mechanisms documented in Figure 5c.

5.3. Results for the *SmS* Phase

[27] The inversion of data at individual stations shows a variability of the Moho depth and reflections attributed to several interfaces at the Moho level. These interfaces sometimes delimit a zone of pronounced reflectivity. In some cases the pronounced *SmS* reflections from the top and bottom of the Moho zone are visible in different azimuths. This

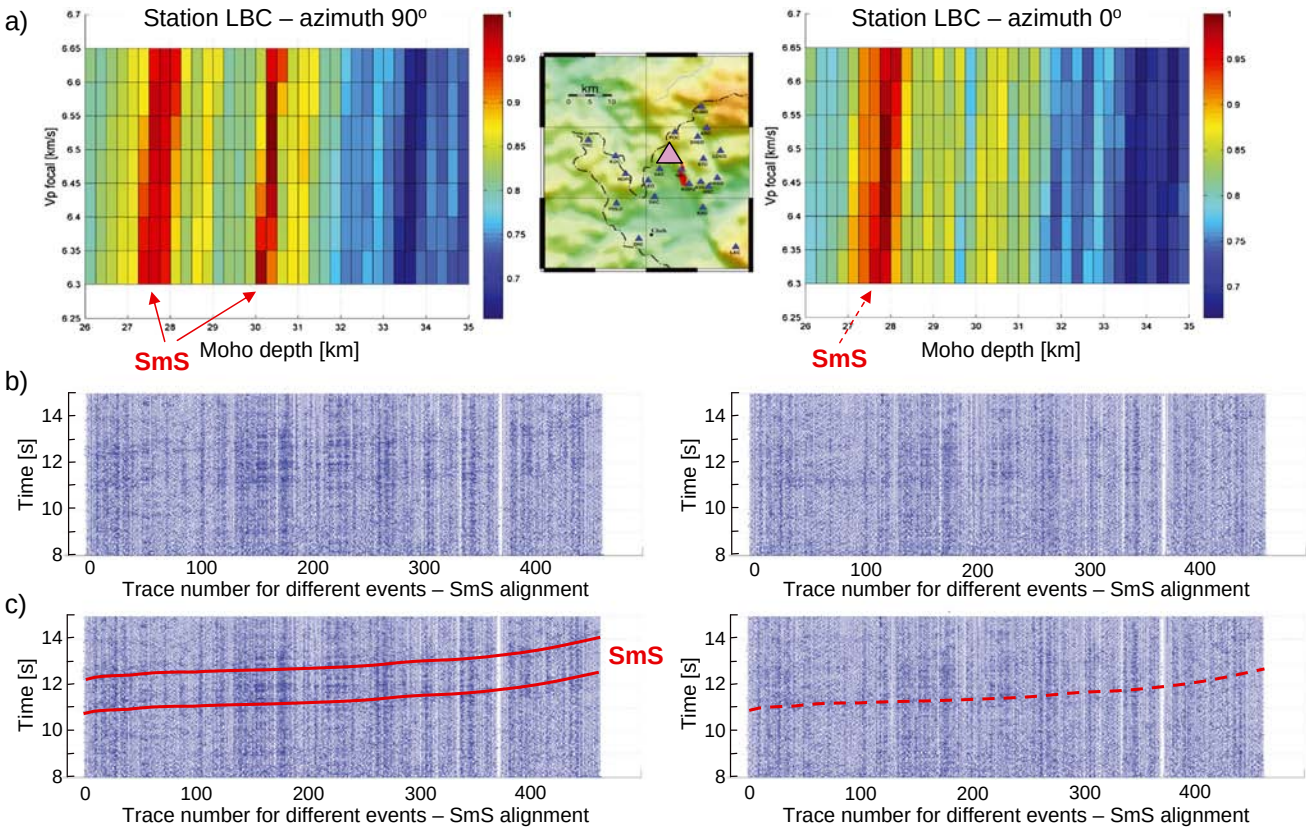

Figure 13. Inversion of the *SmS* reflections for the Moho depth at station LBC. The horizontal velocity records are rotated into azimuths 90° (left panels) and 0° (right panels). Pronounced *SmS* reflections from the top and bottom of the Moho zone are visible in different azimuths. (a) Stacked and inverted *SmS* phases with the grid search algorithm. The scale of the plot is normalized to the maximum amplitude of the stack. (b) Moho reflected *SmS* phases in the data. (c) Moho reflected *SmS* phases in the data with traveltime curves calculated using ray tracing (red lines). Note optimum azimuth of 90° with the most pronounced energy corresponding to the reflections at the depths of 27.50 and 30.25 km (solid red lines). The energy in the perpendicular azimuth of 0° is much weaker and only detects a reflector at a depth of 27.75 km (dashed red line). Position of station LBC in the geographical map is marked by a pink triangle.

is documented in Figure 13 for station LBC. For this station, the optimum azimuth with the most pronounced *SmS* phase has a value of 90° and corresponds to reflections at the depths of 27.50 and 30.25 km. The *SmS* phase in the perpendicular azimuth of 0° is much weaker and detects only a reflector at a depth of 27.75 km.

[28] These findings highlight the importance of the multiazimuthal analysis and its strong impact on the final result. The common analysis of the waveforms in the RTZ coordinate system could easily neglect some *SmS* phases just because of unfavorable radiation pattern or polarization, and the most pronounced interfaces as the Moho depth could easily be misinterpreted. At some stations, the inversion could indicate the bottom of the Moho reflective zone; at other stations, we could get the top of the zone. The interpretation of such results would lead to the Moho depth apparently jumping by about 4 km (the thickness of the Moho reflective zone) when determined from two stations. Since the target area is of a small lateral extent, changes in the Moho depth of 4 km (misinterpretation of a top or bottom of the zone with a simple Moho at different depths) would be quite dramatic and could lead to erroneous tectonic implications. This is illustrated in Figure 10 showing data for station LBC in azimuths of 45° and 120°, which correspond to the *T* and *R* components, respectively. Both components show the interfaces at different depths: at 28 km and 32 km, respectively. Without using the multiazimuthal analysis we would not be able to interpret this phenomenon correctly.

[29] Summarizing the results obtained for all WEBNET stations, we conclude that the inversion of the reflected *SmS* phases at the majority of stations indicates the Moho is a reflective zone rather than a single interface with a sharp velocity contrast. The thickness of the zone varies from 2 to 4 km within the depth range of 27–31.5 km. At a few stations, the inversion yields the Moho with just one or two reflective interfaces with a span of about 1 km. At these stations, this can be interpreted as lower level of reflectivity of the upper and/or bottom interfaces of the zone and rather pronounced strong reflectors in the middle parts of the zone. Details of the interpreted interfaces are summarized in Table 2.

5.4. Misinterpretation of the *SmS* and *PmS* Phases

[30] The grid search algorithm used in the inversion is a powerful tool for finding the Moho depth provided that the identification of the reflected/converted phases is correct.

Table 2. The Moho Interfaces Interpreted From Reflected/Converted *SmS*, *PmP*, and *PmS* Phases at Individual WEBNET Stations in West Bohemia/Vogtland[a]

Station ID	Lat. [deg.]	Lon. [deg.]	Moho Interfaces *SmS* [km]			Moho *PmP* [km]		Moho *PmS* [km]	
NKC	50.2322	12.4471	28.75	29.00[a]	30.50[a]				
KOC	50.2643	12.2328	27.00[b]	29.50[a]	30.50				29.50
KRC	50.3307	12.5295	28.50[b]	29.50[a]	30.50[a]				
LAC	50.0500	12.6242	29.00[b]	31.00[b]	32.00[b]				
SKC	50.1689	12.3602	29.25[a]	30.00					
TRC	50.3023	12.1440	28.00	29.75	31.50[a]				31.25
STC	50.2582	12.5189	29.00	30.00	31.00[b]				
LBC	50.2646	12.4115	27.50	30.50[a]	31.00				
VAC	50.2345	12.3764	27.50	29.75[a]	30.25				
KVC	50.2040	12.5105	29.00	30.75[a]					
KAC	50.1431	12.5172	29.00[a]	30.00	31.25				
POC	50.3211	12.4262		29.75[a]	30.75[a]				
ZHC	50.0697	12.3080		29.50[a]	31.00[a]				29.50
BUBD	50.3821	12.5132	29.50	30.50[a]					30.50
HOPD	50.2241	12.2652	26.75	29.25[a]	30.50			29.50	30.00
HRED	50.2141	12.5652	29.00[b]		31.50[b]				
KOPD	50.2031	12.4741		29.50[a]	30.50[a]	29.50	30.50[a]		
LOUD	50.2771	12.5741	28.00	29.50[a]	30.50[a]				
PLED	50.2071	12.3372	28.00[b]	29.5–30.5[a]	31.00				
POLD	50.1551	12.2352	28.00	29.00[a]	30.50			28.00	29.50
SNED	50.3101	12.5002	27.50[a]	30.50[a]	31.50				28.25
HRC	50.1921	12.5382	29.50[a]	30.50[a]	31.50				

[a]Pronounced interfaces.
[b]Poorly resolved interfaces.

Since we found double *SmS* phases reflected at the top and bottom of the reflective zone, we have to discuss whether these phases were possibly misinterpreted being actually the *SmS* and *PmS* phases reflected and converted at one interface. The correctness of the interpretation can be easily checked by calculating the V_p/V_s ratio from the traveltimes of the *SmS* and *PmS* phases. For example, if the earlier phase from the double *SmS* in Figure 12c (left panel) was the *PmS* we would conclude with a V_p/V_s ratio of about 1.2, which is unrealistic.

[31] On the other hand, we have to also check whether the *SmS* maxima in the grid search inverted for the top of the reflective zone for shallow Moho depths could actually represent the arrivals of the *PmS* phases from the deeper interface. This procedure is documented in Figure 12 (right panels). Station KAC shows a very early maximum of the *SmS* inversion grid at a depth of 26.5 km in an azimuth of 0°. Since this depth is quite shallow, we tested the energy for the *PmS* phase. The ray-tracing calculation confirmed that the energy at these times comes from the *PmS* phase (see data with calculated *PmS* phase in Figure 12c). Therefore, at this station, it is not possible to consider and interpret the *SmS* inversion result (the Moho depth maximum at 26.5 km). This is also in agreement with the synthetics, which show the azimuth of 0° as a direction of missing energy for the *SmS* phases. To conclude, shallower depths representing the top of the Moho reflective zone were interpreted only if we were not able to associate them with the *PmS* phase.

5.5. Moho Depth Inversion of the *PmP* and *PmS* Phases

[32] To better constrain the Moho depth, we can include an interpretation of additional phases. Therefore, the same procedure of the phase identification, multiazimuthal rotation of traces, alignment, stacking, and inversion was applied to reflected *PmP* and converted *PmS* phases if identified in the waveforms observed at the WEBNET stations. The *PmP* phase is usually the second most pronounced reflected phase, being detectable on vertical components. For the majority of the WEBNET stations, this phase is quite close to the direct *S* wave and is thus influenced by the *S* wave coda. Therefore, it is usually difficult to identify the *PmP* phase with a reasonable confidence. The most reliable result was achieved for station KOPD (Figure 14); maybe due to the fact that there is a strongly reflecting interface interpreted at a depth of 30.5 km (see Table 2).

[33] The *PmS* converted phase was identified and inverted for the Moho depth at more stations than the *PmP* phase. This phase was much weaker than the *SmS* phase, so it was usually possible to identify only the strongest Moho *PmS* conversion in the data with no details of the reflective zone. Nevertheless, the *PmS* phase was identified at seven stations, at two of which we were able to identify conversions indicating a reflective zone at the Moho level. Details of the interpreted interfaces from *PmS* phases are summarized in Table 2, an example of the *PmS* interpretation is presented in Figure 15.

[34] The interpretation of the *PmP* and *PmS* phases helped in determining the V_p/V_s ratio and in differentiating the Moho reflective zone. Since we found Moho reflections and conversions for both *P* and *S* waves at some stations, we were able to calculate the mean value of the V_p/V_s ratio in the crust. The V_p/V_s ratio was calculated from doubled reflections at station KOPD as the ratio of delay times between doubled *PmP* phases and between doubled *SmS* phases. It was determined to be 1.73; uncertainty level is estimated to be on the order of 0.02 for the given velocity model.

6. Analysis of Accuracy and Resolution

[35] The accuracy of the Moho depth is influenced by several factors. First, the accuracy is affected by an alignment of

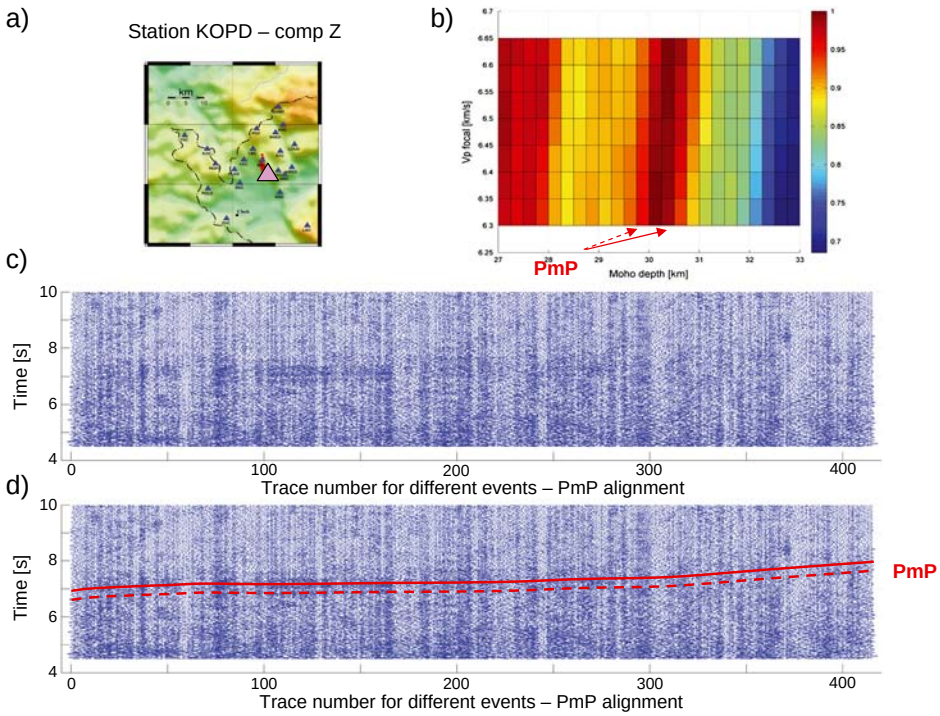

Figure 14. Inversion of the *PmP* reflections for the Moho depth at station KOPD. Vertical velocity records. (a) Map of the area with station KOPD marked by a pink triangle. (b) Stacked and inverted *PmP* phases with the grid search algorithm. The scale of the plot is normalized to the maximum amplitude of the stack. Note maximum Moho depth at 30.25 km. Inversion extreme at around 27 km is attributed to the *S* wave coda. (c) Moho reflected *PmP* phases in the data. Note strong amplitudes of fading *S* wave coda at earlier arrival times. (d) Moho reflected *PmP* phases in the data with traveltime curves calculated using ray tracing. Note strong reflector at a depth of 30.5 km (solid red line) and a weak reflection at a depth of 29.5 km (dashed red line) visible in the data and not so pronounced in the inversion.

individual waveforms used for stacking. Since the sampling frequency is 250 Hz and the arrival times of the direct *P* and *S* waves are measured very precisely with the accuracy of less than 4 and 10 ms, respectively, the error produced by the alignment is insignificant. Second, the accuracy depends on the stacking procedure used. In stacking, the waveforms are not summed at each sample, but the waveforms are divided into intervals of 150 ms, numerically integrated, and summed. This produces higher amplification and better resolution of inverted phases. Since ~130 ms represents a Moho depth change of 0.250 km, this leads to the Moho determination of the order of 0.25 km. Third, the accuracy is influenced by the size of steps of parameters used in the grid search inversion and by the shape of the final stack of the data. The grid step for the Moho depth was chosen to be 0.25 km, which suggests the limiting resolution of the results. Since the stack was not always sharp but blurred in some cases, the overall depth resolution is lower, of the order of 0.5 km.

[36] The accuracy of the Moho depth is also influenced by the Earth's crust velocity model used for locations of the earthquakes and for calculating the travel times of the direct and reflected/converted waves. For the applied velocity/depth profile (Table 1) we obtained the Moho depth within the range of 27–31.5 km. Higher overall crustal velocities would result in deeper Moho and smaller crustal velocities would result in shallower Moho. As an example, a 5% velocity change results in ~1.5 km Moho depth difference. However, the variations of the Moho depth among individual stations are more accurate. They are insensitive to the velocity model and their accuracy is about 0.5 km similarly as the overall resolution of the inversion method.

[37] The retrieved V_p/V_s ratio is independent on the velocity model used. Since we were working with both *P* and *S* waves independently, we could calculate the overall crustal V_p/V_s value based on the results of the inversion to match the results from the *S* and *P*-wave interpretations. The V_p/V_s ratio was calculated to be 1.73 with an uncertainty level on the order of ~0.02. However, only few stations showed Moho converted *PmS* phases or *PmP* reflected phases, so the determined V_p/V_s ratio is not representative for the whole region and more stations with identified *P* phases could refine this value.

7. Discussion

[38] Waveforms from local microearthquakes represent an important source of data for crustal studies. Not only because the microseismicity produces large datasets ideal for stacking, but also because microearthquakes are usually located much deeper than the explosions used in active seismic experiments. In consequence, the waveforms of microearthquakes are simple and not as affected by the low-velocity subsurface layers as the waveforms of the explosions. Also high-frequency seismic waves generated by microearthquakes

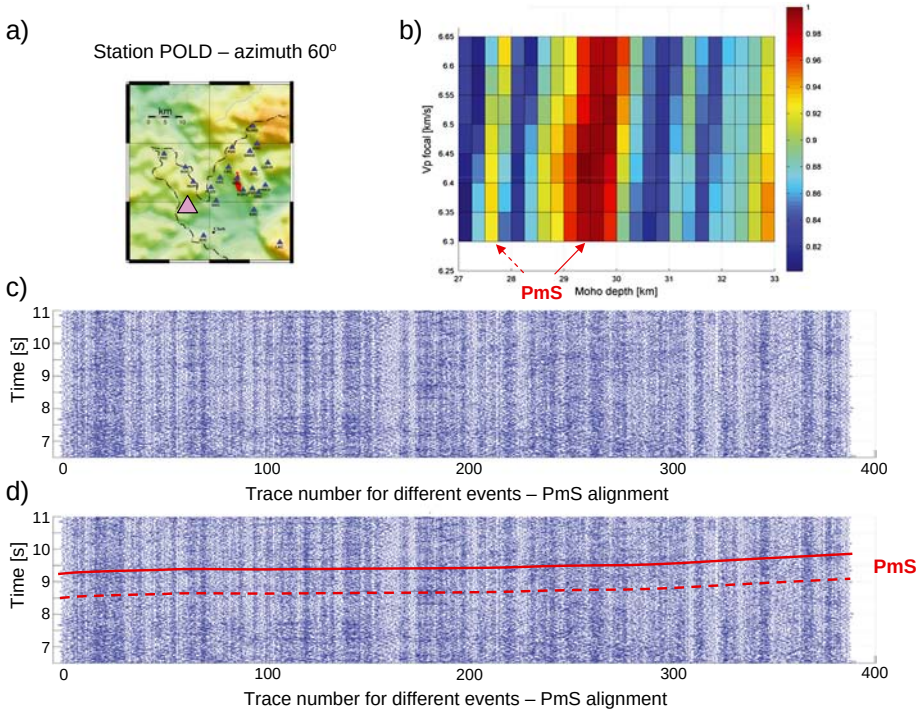

Figure 15. Inversion of the *PmS* reflections for the Moho depth at station POLD. The horizontal velocity records are rotated into azimuths 60°. (a) Map of the area with station POLD marked by a pink triangle. (b) Stacked and inverted *PmS* phases with the grid search algorithm. The scale of the plot is normalized to the maximum amplitude of the stack. (c) Moho converted *PmS* phases in the data. (d) Moho reflected *PmS* phases in the data with traveltime curves calculated using ray tracing. Note strong convertor at a depth of 29.5 km (solid red line) and a weak convertor at a depth of 27.5 km (dashed red line) visible in the data and not so pronounced in the inversion.

may bring higher resolution in the determination of depth and topography of crustal interfaces.

[39] On the other hand, analysis of microseismic data is specific and it requires new methods of processing. The wave amplitudes and their polarization are quite sensitive to focal mechanisms and to source-receiver geometry, so the waveforms can be extremely variable. Consequently, the amplitudes of the reflected/converted phases do not depend just on the contrasts at interfaces in the model but also on the earthquake source and its radiation pattern. Therefore, a parallel processing of an extensive dataset rotated into many azimuths is needed to reliably detect and enhance the resolution of the reflected/converted phases scattered at structural interfaces.

[40] In this paper, we used the microseismic data for studying the Moho depth and its topography in the West Bohemia/Vogtland region. The data were processed with a combination of several tools: (1) ray tracing in order to calculate the arrival times of reflected/converted Moho phases, (2) analysis of the R/T coefficients of the Moho phases in order to assess their amplitudes and resolution in real waveforms, (3) synthetic modeling of full waveforms using the discrete wave-number method, (4) data rotation into multi-azimuthal sections, (5) data alignment and stacking to amplify the Moho phases, and (6) the grid search algorithm as the robust inversion method. Application of these tools enabled us to determine lateral variation of the Moho depth and to reveal details of the crust/mantle transition.

[41] The results indicate that the Moho in the target area is a wide reflective zone rather than a single sharp interface. The thickness of the zone varies from 2 to 4 km within the depth range of 27–31.5 km with the V_p/V_s ratio of 1.73 and it is delimited by reflections from its top and bottom boundaries. Figure 16 shows 3-D image of interpolated Moho reflective interfaces; Figure 17 presents the interpolated Moho depth variations for the top of the reflective

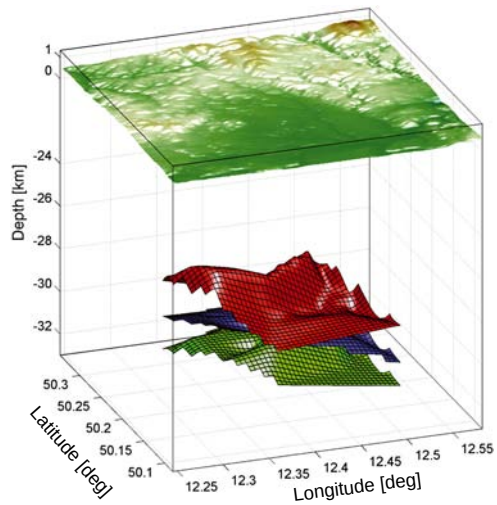

Figure 16. 3-D image of the Moho reflective interfaces.

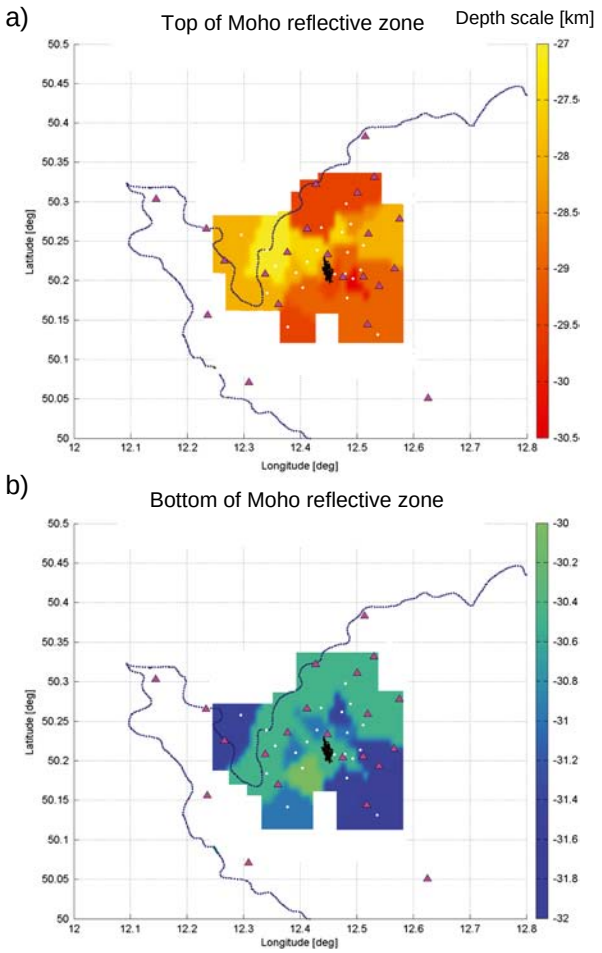

Figure 17. (a) Moho topography for the top of the reflective zone. (b) Moho topography for the bottom of the reflective zone. White dots mark the actual positions of detected Moho reflections (i.e., midpoints between stations and sources); magenta triangles represent positions of stations; black dots mark epicenters.

zone as well as for its bottom. The actual positions of detected Moho reflections (i.e., midpoints between stations and sources) are marked by white dots. The upper interface is at a depth of 27–29 km and deepens toward the middle of the study area with NNE-SSW trend. The bottom interface is at a depth of 30–31.5 km, with the shallowest part also trending NNE-SSW across the center of the study area. The NNE-SSW direction characterizes a direction of the narrowest part of the reflective zone with a thickness of only 1–1.5 km. In this case, strong reflecting interfaces at the top and bottom are quite close to each other. However, these two close interfaces may not represent the top and bottom of the reflective zone, but it may involve strong reflectors within the zone that mask less pronounced reflectivity from shallower or deeper parts above and below these two strong reflectors.

[42] To avoid confusion and complete the discussion about the existence of the Moho reflective zone, we have to discuss whether the multiple *SmS* phases reflected at the top and bottom of the reflective zone are not misinterpreted being in fact just split *S* waves reflected at a single interface in an anisotropic crust. In our approach, we did not consider the seismic anisotropy of the crust, although *Vavryčuk* [1993] and *Vavryčuk and Bouškova* [2008] showed that the crust is anisotropic in this region with the anisotropy strength of about 4–6% for the *S* waves. Hence, the assumption of isotropy is not valid in West Bohemia and anisotropy can affect the obtained results. However, we believe the anisotropy effects do not invalidate our results. We conclude that the interpretation of data in favor of a single strong Moho discontinuity in anisotropic crust is not plausible for the following reasons. First, the delay times between the doubled *SmS* phases reach values of up to 1.5 s corresponding to *S*-wave anisotropy strength of 10% along the whole ray path, which is a rather high and unrealistic value for the crust. Second, if the Moho was a single strong-contrast interface, the data sections should consistently show single *PmP* reflections. However, the time sections for the station KOPD show that the doubled phases are present at the *SmS* as well as the *PmP* phases. From this point of view, anisotropy does not satisfactorily explain complexities in the reflected/converted Moho phases. Nevertheless, anisotropy can still have some impact and can complicate the pattern of the Moho reflections and conversions in the waveforms.

[43] The Moho reflective zone in West Bohemia/Vogtland is not a new phenomenon, but it is also reported in other studies from this region. Similar results were obtained along the refraction profile CEL09 by *Hrubcová et al*. [2005], who interpreted the Saxothuringian unit with a highly reflective top of the lower crust at a depth of 27–28 km. A high-velocity layer at the base of the crust was also found along deep reflection profiles MVE-90 and GRANU'95 [*DEKORP Research Group*, 1994; *Enderle et al*., 1998]. *Kampfová et al*. [2007] interpreted the Moho in West Bohemia from quarry blasts and found scattered reflections from depths within the range of 29.5–31.5 km. Possible reflective lower crust has also been reported as a phenomenon observed in broader Variscan areas: by *Malinowski et al*. [2005] beneath the Silesian Block in SE Poland, by *Hrubcová and Środa* [2008] at the eastern edge of the Bohemian Massif, or by *Hrubcová et al*. [2010] in the Saxothuringian region. Also, the receiver function studies provide, to some extent, an explanation with the reflective zone. This was discussed by *Hrubcová and Geissler* [2009]. Their joint modeling of receiver functions and refraction profiling disclosed that the lower crustal zone in the West Bohemia/Vogtland area can be 4–5 km thick with the top at a depth of 28 km where high reflectivity obscured the Moho reflections at a depth of 32–33 km.

8. Tectonic Implications

[44] The most common explanation of a lower crustal reflectivity is the presence of densely spaced thin layers of high and low velocities represented, for example, by alternating mafic/ultra mafic material. Also, the reflective zone can be attributed to subhorizontal lamina of dense mafic rocks or melt within felsic granulites or garnet pyroxene granulites [*Handy and Streit*, 1999; *Morozov et al*., 2001]. In addition, the lower crustal reflectivity can be affected by solidified intrusions most probably of amphibolite-rich composition, possibly stretched and arranged horizontally during a postorogenic extension. Another explanation may involve a change of material with different metamorphic grade alternating from granulite to

amphibolite facies depending on metamorphic grade, composition and the *P-T* conditions [*Furlong and Fountain*, 1986; *Hurich et al*., 2001]. Such metamorphic processes are associated with lithospheric plate boundaries, where the interactions between plates can produce sufficient heat for metamorphism of the crustal rocks on a large scale. *Warner* [1990] discussed shear zones in the lower continental crust explaining them as layers with high fluid content. Since fluids in West Bohemia/Vogtland, though shallower, are discussed as a potential triggering factor for the earthquake swarms [e.g., *Vavryčuk*, 2002; *Horálek et al*., 2000], there might be some affinity with deep tectonics.

[45] The deep tectonic processes must also be responsible for the varying thickness of the Moho reflective zone in the West Bohemia/Vogtland region, which is situated in the transition zone between different Variscan structural units [*Babuška et al.*, 2007]. The Moho reflective zone is thin in the NNE-SSW direction, possibly indicating an association with the western termination of the Eger Rift trending in a similar NE-SW direction. Such interpretation may involve deeper seated tectonics at the contact of the three tectonic units as discussed, e.g., by *Plomerová et al*. [2007]. Alternatively, there could be an association with an active fault system trending N-S [*Bankwitz et al*., 2003] encompassing the fault activated during the interpreted 2008 swarm. However, since the information on the Moho topography is local, we are not able to reliably draw more specific tectonic conclusions. To elucidate this problem in future studies, we would suggest to include more distant stations in the analysis.

[46] **Acknowledgments.** This research was supported by the Grant Agency of the Czech Republic, grant P210/10/2063, and by the Grant Agency of the Academy of Sciences of the Czech Republic, grant IAA300120801. Data acquisition was supported by the project of large research infrastructure CzechGeo, grant LM2010008. This work was also sponsored by the research project SH 55/11-1 funded by DFG (Deutsche ForschungsGemeinshaft). The authors are grateful to Fateh Bouchaala for his help with data processing, and Prof. G. Randy Keller, an anonymous reviewer, and the associate editor for their valuable comments and suggestions on manuscript improvement.

References

Babuška, V., J. Plomerová, and T. Fischer (2007), Intraplate seismicity in the western Bohemian Massif (central Europe): a possible correlation with a paleoplate junction, *J. Geodynamics*, *44*, 149–159, doi:10.1016/j.jog.2007.02.004.

Bankwitz, P., G. Schneider, H. Kämpf, and E. Bankwitz (2003), Structural characteristics of epicentral areas in Central Europe: study case Cheb Basin (Czech Republic), *J. Geodynamics*, *35*, 5–32, doi:10.1016/S0264-3707(02)00051-0.

Behr, H.-J., H.-J. Dürbaum, and P. Bankwitz (1994), Crustal structure of the Saxothuringian Zone: Results of the deep seismic profile MVE-90 (East), *Z. Geol. Wiss.*, *22*(6), 647–769.

Bouchon, M. (1981), A simple method to calculate Green's functions for elastic layered media, *Bull. Seis. Soc. Am.*, *71*, 959–971.

Brückl, E., et al. (2007), Crustal structure due to collisional and escape tectonics in the Eastern Alps region based on profiles Alp01 and Alp02 from the ALP 2002 seismic experiment, *J. Geophys. Res.*, *112*, B06308, doi:10.1029/2006JB004687.

DEKORP Research Group (1988), Results of deep reflection seismic profiling in the Oberpfalz (Bavaria), *Geophys. J. Int.*, *89*, 353–360, doi:10.1111/j.1365-46X.1987.tb04430.x.

DEKORP Research Group (1994), The deep reflection seismic profiles DEKORP 3/MVE-90, *Z. Geol. Wiss.*, *22*(6), 623–824.

Enderle, U., K. Schuster, C. Prodehl, A. Schultze, and J. Briebach (1998), The refraction seismic experiment GRANU'95 in the Saxothuringian belt, southeastern Germany, *Geophys. J. Int.*, *133*, 245–259.

Fischer, T., and J. Horálek (2003), Space-time distribution of earthquake swarms in the principal focal zone of the NW Bohemia/Vogtland seismoactive region: period 1985-2001, *J. Geodynamics*, *35*, 125–144.

Fischer, T., J. Horálek, J. Michálek, and A. Boušková (2010), The 2008 West Bohemia earthquake swarm in the light of the WEBNET network, *J. Seismology*, *14*, 665–682.

Furlong, K. P., and D. M. Fountain (1986), Continental crustal underplating: thermal considerations and seismic-petrologic consequences, *J. Geophys. Res.*, *91*, 8285–8294.

Geissler, W. H., H. Kämpf, R. Kind, K. Klinge, T. Plenefisch, J. Horálek, J. Zedník, and V. Nehybka (2005), Seismic structure and location of a CO2 source in the upper mantle of the western Eger rift, Central Europe, *Tectonics*, *24*, TC5001, doi:10.1029/2004TC001672.

Grad, M., A. Guterch, S. Mazur, G. R. Keller, A. Špičák, P. Hrubcová, and W. H. Geissler (2008), Lithospheric structure of the Bohemian Massif and adjacent Variscan belt in central Europe based on profile S01 from the SUDETES 2003 experiment, *J. Geophys. Res.*, *113*, B10304, doi:10.1029/2007JB005497.

Handy, M. R., and J. E. Streit (1999), Mechanics and mechanism of magmatic unerplating: inferences from mafic veins in deep crustal mylonite, *Earth Planet. Sci. Lett.*, *165*, 271–286.

Heuer, B., W. H. Geissler, R. Kind, and H. Kämpf (2006), Seismic evidence for asthenospheric updoming beneath the western Bohemian Massif, central Europe, *Geophys. Res. Lett.*, *33*, L05311, doi:10.1029/2005GL025158.

Horálek J., T. Fischer, A. Boušková, J. Michálek, and P. Hrubcová (2009), The West Bohemian 2008-earthquake swarm: when, where, what size and data, *Stud. Geophys. Geod.*, *53*, 351–358, doi:10.1007/s11200-009-0024-8.

Horálek, J., T. Fischer, A. Boušková, and P. Jedlička (2000), The Western Bohemia/Vogtland Region in the Light of the Webnet Network, *Stud. Geophys. Geod.*, *44*, 107–125.

Hrubcová, P., P. Środa, A. Špičák, A. Guterch, M. Grad, G. R. Keller, E. Brückl, and H. Thybo (2005), Crustal and uppermost mantle structure of the Bohemian Massif based on CELEBRATION 2000 data, *J. Geophys. Res.*, *110*, B11305, doi:10.1029/2004JB003080.

Hrubcová, P., P. Środa, and CELEBRATION 2000 Working Group (2008), Crustal structure at the easternmost termination of the Variscan belt based on CELEBRATION 2000 and ALP 2002 data, *Tectonophysics*, *460*, 55–75, doi:10.1016/j.tecto.2008.07.009.

Hrubcová, P., and W. H. Geissler (2009), The Crust-Mantle Transition and the Moho beneath the Vogtland/West Bohemian Region in the Light of Different Seismic Methods, *Stud. Geophys. Geod.*, *53*, 275–294.

Hrubcová, P., P. Środa, M. Grad, W. H. Geissler, A. Guterch, J. Vozár, E. Hegedüs, and Sudetes 2003 Working Group (2010), From the Variscan to the Alpine Orogeny: crustal structure of the Bohemian Massif and the Western Carpathians in the light of the SUDETES 2003 seismic data, *Geophys. J. Int.*, doi:10.111/j.1365-246X.2010.04766.x.

Hurich, C. A., S. J. Deemer, A. Indares, and M. Salisbury (2001), Compositional and metamorphic controls on velocity and reflectivity in the continental crust: an example from the Grenville Province of eastern Québec, *J. Geophys. Res.*, *106*, 665–682.

Kampfová, H., J. Málek, and O. Novotný (2007), Moho reflections from strong near quarry blasts: an example for the central ore mountains, Czech Republic, *Acta Geodyn. Geomater.*, *4*, 11–21.

Málek, J., J. Horálek, and J. Janský (2005), One-dimensional qP-wave velocity model of the upper crust for the West Bohemia/Vogtland earthquake swarm region, *Stud. Geophys. Geod.*, *49*, 501–524.

Malinowski, M., A. Żelaźniewicz, M. Grad, A. Guterch, T. Janik, and CELEBRATION Working Group (2005), Seismic and geological structure of the crust in the transition from Baltica to Palaeozoic Europe in SE Poland – CELEBRATION 2000 experiment, profile CEL02, *Tectonophysics*, *401*, 55–77, doi:10.1016/j.tecto.2005.03.011.

Matte, P., H. Maluski, P. Rajlich, and W. Franke (1990), Terrane boundaries in the Bohemian Massif: Result of large-scale Variscan shearing, *Tectonophysics*, *177*, 151–170, doi:10.1016/0040-1951(90)90279-H.

Morozov, I. B., S. B. Smithson, J. Chen, and L. S. Hollister (2001), Generation of new continental crust and terrane accretion in Southeastern Alaska and Western British Columbia: constraints from P- and S-wave wide-angle seismic data (ACCRETE), *Tectonophysics*, *341*, 49–67.

Plomerová, J., U. Achauer, V. Babuška, L. Vecsey, and Bohema W. G. (2007), Upper mantle beneath the Eger Rift (Central Europe): plume or asthenosphere upwelling? *Geophys. J. Int.*, *169*, 675–682, doi:10.1111/j.1365-246X.2007.03361.x.

Prodehl, C., S. Mueller, and V. Haak (1995), The European Cenozoic Rift System, in *Continental rifts: evolution, structure, tectonics*, edited by K. H. Olsen, *Developments in Geotectonics*, Elsevier, 133–212.

Tomek, Č., V. Dvořáková, and S. Vrána (1997), Geological interpretation of the 9HR and 503 M seismic profiles in Western Bohemia, in *Geological model of Western Bohemia related to the KTB borehole in Germany*, edited by S. Vrána and V. Štědrá, *J. Geol. Sci., Geology*, *47*, 43–50.

Vavryčuk, V. (1993), Crustal anisotropy from local observations of shear-wave splitting in West Bohemia, Czech Republic, *Bull. Seism. Soc. Am.*, *83*, 5, 1420–1441.

Vavryčuk, V. (2002). Non-double-couple earthquakes of January 1997 in West Bohemia, Czech Republic: Evidence of tensile faulting, *Geophys. J. Int.*, *149*, 364–373, doi:10.1046/j.1365-246X.2002.01654.x.

Vavryčuk, V., and A. Bouškova (2008), S-wave splitting from records of local micro-earthquakes in West-Bohemia/Vogtland: An indicator of complex crustal anisotropy, *Stud. Geophys. Geod.*, *52*, 631–650.

Vavryčuk, V. (2011a), Detection of high-frequency tensile vibrations of a fault during shear rupturing: Observations from the 2008 West Bohemia swarm, *Geophys. J. Int.*, *186*, 1404–1414, doi:10.1111/j.1365-246X.2011.05122.x.

Vavryčuk, V. (2011b), Tensile earthquakes: Theory, modeling, and inversion, *J. Geophys. Res.*, *116*, B12320, doi:10.1029/2011JB008770.

Vavryčuk, V. (2011c), Principal earthquakes: Theory and observations for the 2008 West Bohemia swarm, *Earth Planet. Sci. Lett.*, *305*, 290–296, doi:10.1016/j.epsl.2011.03.002.

Warner, M. R. (1990), Basalts, water or shear zones in the lower continental crust? *Tectonophysics*, *173*, 163–173.

Weinlich, F. H., K. Brauer, H. Kämpf, G. Strauch, J. Tesar, S. M. Weise (1999), An active subcontinental mantle volatile system in the western Eger rift, Central Europe: Gas flux, isotopic (He, C, and N) and compositional fingerprints, *Geochim. Cosmochim. Acta*, *63*, 3653–3671, doi:10.1016/S0016-7037(99)00187-8.

Wilde-Piórko, M., J. Saul, and M. Grad (2005), Differences in the crustal and uppermost mantle structure of the Bohemian Massif from teleseismic receiver functions, *Stud. Geophys. Geod.*, *49*, 85–107.